

Distributed context-dependent choice information in mouse posterior cortex

Javier Orlandi

University of Calgary

Mohammad Abdolrahmani

RIKEN Center for Brain Science

Ryo Aoki

RIKEN Center for Brain Science

Dmitry Lyamzin

RIKEN Center for Brain Science <https://orcid.org/0000-0002-7082-2902>

Andrea Benucci (✉ andrea@benuccilab.net)

RIKEN Center for Brain Science <https://orcid.org/0000-0002-7698-6289>

Article

Keywords: recurrent neural network, posterior cortex, decision computations

Posted Date: September 20th, 2021

DOI: <https://doi.org/10.21203/rs.3.rs-907578/v1>

License:  This work is licensed under a Creative Commons Attribution 4.0 International License.

[Read Full License](#)

1 Distributed context-dependent choice information 2 in mouse posterior cortex

Javier Orlandi¹, Mohammad Abdolrahmani¹, Ryo Aoki¹, Dmitry Lyamzin¹, Andrea Benucci^{1,2*}

¹RIKEN Center for Brain Science, 2-1 Hirosawa, Wako-shi, Saitama 351-0198, Japan

²University of Tokyo, Graduate School of Information Science and Technology, Department of Mathematical Informatics, 1-1-1 Yayoi, Bunkyo City, Tokyo 113-0032, Japan

*Corresponding authors: andrea.benucci@riken.jp (A.B)

Abstract

3 Choice information appears in multi-area brain networks mixed with sensory, motor, and cognitive
4 variables. In the posterior cortex—traditionally implicated in decision computations—the presence,
5 strength, and area specificity of choice signals are highly variable, limiting a cohesive understanding of
6 their computational significance. Examining the mesoscale activity in the mouse posterior cortex during a
7 visual task, we found that choice signals defined a decision variable in a low-dimensional embedding space
8 with a prominent contribution along the ventral visual stream. Their subspace was near-orthogonal to
9 concurrently represented sensory and motor-related activations, with modulations by task difficulty and
10 by the animals' attention state. A recurrent neural network trained with animals' choices revealed an
11 equivalent decision variable whose context-dependent dynamics agreed with that of the neural data. Our
12 results demonstrated an independent, multi-area decision variable in the posterior cortex, controlled by
13 task features and cognitive demands, possibly linked to contextual inference computations in dynamic
14 animal–environment interactions.

Introduction

15 The search for the neural basis of perceptual decisions has been recently accelerated by important
16 technological advances for monitoring and perturbing the activity of large neuronal populations across
17 multiple areas during complex behaviors^{1,2}. The view emerging from these studies challenges the simple
18 interpretation of discrete neural modules that selectively encode sensory, decisional, or motor
19 processes^{3,4}, revealing mixed representations within and across neurons⁵. Mixed selectivity suggests
20 complex interactions of task and behavioral variables with decision information^{6–8}, with the prominence
21 of decision signals being influenced by the stimulus-coding strength of neurons^{9,10}, the correlation
22 properties of the network^{11–13}, and modulatory signals associated with changeable states of attention¹⁴.
23 Attention can also contextually enable, route, and gate decision-related information¹⁵. Together with the

24 area location in the sensory hierarchy^{16,17}, even the strategy used by an animal to solve a task can affect
25 the detectability of decision signals¹⁸.

26 These observations have been consistently reported across mammalian species, with mouse
27 models playing an increasingly prominent role in decision-making studies in view of the abundant tools
28 available for the dissection of neural circuits¹⁹. Several recent mouse works have demonstrated that in
29 occipital, parietal, and frontal cortices mixed with decision signals are task-instructed and uninstructed
30 movement-related activations that elicit large-amplitude responses^{20–23}. Disentangling movement and
31 other mixed variables has proved to be challenging, depending also on the characteristics of the task
32 design and demands. For instance, in tasks with freely moving animals or in virtual-reality navigation tasks
33 with head fixation, motor signals continuously affect cortex-wide networks, with head and body orienting
34 movements predictive of choice²⁴. Even when movements are limited, as in head-fixed tasks with no
35 navigation, movements of the body extracted from videography can be predictive of choice^{25,26}.
36 Furthermore, the distribution of movement, perceptual, and decision variables over cortical space is not
37 constrained by area boundaries (e.g., retinotopically defined), thus challenging a precise localization of
38 these signals^{21,27}. Task demands, such as the need to accumulate sensory evidence^{28–37} or to engage short-
39 term memory mechanisms^{20,25,28,38–48}, and the targeted sensory modality^{20,32,37,49}, all profoundly affect the
40 strength and multi-network distribution of choice signals (reviewed in Supplementary Table 1). These
41 complex dependences have been demonstrated in a series of inactivation studies that have profoundly
42 changed our view of posterior parietal networks in decision computations. Inactivation of the posterior
43 parietal cortex (PPC) can affect decisions indirectly, for example, by removing “irrational” biases^{41,43,50},
44 impairing memory-related components^{30,38}, or affecting the categorization of novel but not familiar
45 stimuli⁵⁰. In all these works, effect size is critically dependent on the inactivation time relative to the
46 sensory cue^{35,36,42,43,45}. These observations cohere with PPC inactivation studies in non-human
47 primates^{51,52}. However, in visual tasks that minimized short-term memory, novelty, navigation, and
48 evidence accumulation components (hereafter, “visually guided tasks” for brevity), visual areas in the
49 posterior cortex did not seem to carry any significant choice information^{26,53–55}. This may be related to the
50 low cognitive demands of the tasks^{50,54} or to the spatial locality of the signals analyzed, unable to capture
51 choice information if sparsely represented across neurons and broadly distributed in posterior multi-area
52 networks⁵⁶. Therefore, when focusing on perceptual aspects of the decision-making process, mouse
53 studies have questioned the representation of choice information in the posterior cortex during visually
54 guided behaviors. This represents a departure from some primate studies that instead have identified
55 choice information even in early visual areas during visually guided tasks^{9,56–62}.

56 Here, we sought to investigate the presence and representation of choice information in the
57 mouse posterior cortex by introducing two novel elements: one for the experimental design and one for
58 the data analysis. First, we trained animals in a complex variant of an orientation discrimination task⁶³,
59 aiming to maximize cognitive demands based on perceptual information but without the need to
60 introduce memory, novelty, navigation, or evidence accumulation components. Second, we applied a
61 tensor decomposition method⁶⁴ combined with activity-mode analysis⁶⁵ on mesoscale recordings of the
62 posterior cortex (imaging of GCaMP signals); this analysis enabled the detection of signals even if sparsely

63 represented among neurons and distributed across broad regions irrespective of classic area boundaries,
64 such as those defined by retinotopic mapping⁶⁴.

Results

65 Mesoscale imaging of the posterior cortex during a discrimination task

66 Using an automated setup featuring voluntary fixation of the animals' heads⁶⁶ (Fig. 1a), we trained mice
67 ($n = 7$) to carry out a complex version of a two-alternative forced choice (2AFC) orientation discrimination
68 task⁶³. The animals had to use their front paws to rotate a toy wheel⁶⁷ that controlled the horizontal
69 position of two circular grating stimuli presented on a screen positioned in front of them. Each stimulus
70 was presented at monocular eccentricities with orientations that varied from trial to trial. To obtain a
71 water reward, mice had to shift the stimulus most similar to a learned target orientation to the center of
72 the screen (Fig. 1b-c), with the actual target orientation rarely shown to the animal. Therefore, difficulty
73 had an invariance to absolute orientations, which had to be ignored by the animal and depended only on
74 the relative orientation between the two stimuli⁶³. After reaching performance levels above 75 % correct
75 (Fig. 1d), we used a macroscope to image mesoscale GCaMP responses in 10 posterior cortical areas (Fig.
76 1e; Methods). In individual trials, the neural activity was highly variable, with response activity associated
77 with the onset of visual stimuli and movements of the limbs, trunk, and eyes, as recently described²² (Fig.
78 1f).

79 Decomposition of neural responses

80 To extract different variables from the neural signal and map them to defined cortical regions, we adopted
81 a recent variant of non-negative matrix factorization—locaNMF⁶⁴. This decomposition method identifies
82 tensor components associated with specified *seeding* regions. When seeding on a given area, locaNMF
83 decomposes the signal into a sum of separable spatial-temporal tensors, with spatial components
84 constrained by the seeding region and temporal components representing the scaling amplitudes of the
85 spatial components. These temporal vectors are potentially more informative than a single vector
86 computed as the average across spatial locations (pixels) within a given area⁶⁴. We aligned all imaging
87 sessions according to the Allen Common Coordinate Framework⁶⁸ (Fig. 2a), and seeded the initial spatial
88 decomposition using 10 large regions centered on retinotopically identified areas that extended
89 significantly beyond area boundaries (Supplementary Fig. 1a-b). Consistent with the initial seeding, the
90 factorization typically converged toward components with peak amplitudes within individual retinotopic
91 areas (Fig. 2b). Depending on the seeding region, associated temporal components differentially
92 emphasized sensory or behavioral variables; for instance, when seeding on the primary visual cortex, the
93 largest component (in explained variance, EV) clearly highlighted a stimulus-evoked response (Fig. 2b).
94 The largest components within the parietal regions⁶⁹ showed negligible visually driven responses and
95 strong movement-related activations (Fig. 2b). Each locaNMF component provided significant explanatory
96 power, with each main component of a seeding area contributing, on average, 9.6 % of the total explained
97 variance (Supplementary Fig. 1c). By contrast, the first PCA component contributed, on average,
98 approximately 85 % of EV, being strongly influenced by large amplitude movement-related activations²⁰.

99 For each area, the number of components significantly contributing to the EV (Methods) was not directly
100 proportional to surface area; for instance, areas AL and L had commensurate surface area and contributed
101 similarly to the overall EV, but L required about twice as many components as AL (Supplementary Fig. 1d-
102 g), in agreement with the different cortical localizations of task and behavioral variables.

103 To identify these variables in locaNMF components, we defined *state axes* in a multi-dimensional
104 space of component activations (Fig. 2c). This approach further reduced the dimensionality of the data by
105 isolating activity dimensions that linearly discriminated pairs of variables. To examine components
106 associated with visual signals, we defined a stimulus axis as the difference between vectorized tensor
107 components in the presence and absence of the stimulus (Methods). This axis remained stable after the
108 stimulus' appearance (Supplementary Fig. 2a), and the projected locaNMF components deviated from the
109 baseline about 200 ms after stimulus onset (Fig. 2d). We quantified the time-dependent increase of
110 detectability of stimulus components using a d' discriminability measure, which can be linked to Fisher
111 information^{70,71}, that bounds the variance for estimating a population-encoded parameter. Different areas
112 contributed to d' with different weights, reaching values greater than one at the peak of stimulus response
113 (Fig. 2d; 1.38 ± 0.13 , mean \pm standard error, s.e.). Using only the LocaNMF components from a particular
114 seeding region allowed us to also quantify the relative contribution of that area to the d' discriminability.
115 For the stimulus variable, the primary and secondary visual cortices (V1, L) had the largest discriminability
116 ($d' = 1.10 \pm 0.09$ and 1.12 ± 0.13 , respectively), followed by area AL ($d' = 0.51 \pm 0.06$). When attempting
117 to discriminate the orientation of the contralateral visual stimulus, no area carried sufficient information,
118 even for the most dissimilar orientation pairs (Supplementary Fig. 3), as expected from the lack of
119 orientation domains in the mouse visual cortex⁷² and the mesoscale imaging spatial resolution. In control
120 experiments, we used a dual-wavelength imaging approach to quantify the effect of the hemodynamic
121 component⁷³. Measurements of the calcium-independent GCaMP fluorescence showed that locaNMF
122 components, state axes, and discriminability values were not significantly affected by the hemodynamic
123 signal (Supplementary Fig. 4).

124 Besides bottom-up visual inputs, imaged posterior regions reflected activations associated with
125 general movements of the body and eyes²¹. Therefore, we defined state axes associated with wheel and
126 eye movements. Projections onto these axes resulted in high discriminability of both types of movements
127 (Fig. 2e-f; peak $d' = 1.29 \pm 0.07$ and 0.94 ± 0.08 for wheel and eye movements, respectively). Area-specific
128 projections highlighted larger contributions by anterior-medial areas (Fig. 2e-f; Supplementary Fig. 2b-c),
129 with d' values increasing before or coincidentally with the detection of movements, suggesting pre-motor
130 contributions, e.g., corollary discharges⁷⁴, and reaching values greater than one after movement
131 execution.

132 We also identified aspects of the variability in locaNMF components that depended on the
133 attention state of the animal. Underlying changes in sustained attention can be both task-related (e.g.,
134 engagement or motivational state) and task-independent components (e.g., arousal or alertness)^{75,76}.
135 Accordingly, in individual sessions, we observed fluctuations in performance that correlated with changes
136 in pupil dilations and reaction times (Supplementary Fig. 5a-b)—two biomarkers associated with changes
137 in sustained attention^{21,77}. Based on the variability in pupil diameter (Methods), we defined a state axis

138 that discriminated between states of high and low sustained attention (Fig. 2g). Associated d' values
139 deviated significantly from zero largely before stimulus onset (after imposed zero discriminability at trial
140 onset; see Methods). Discriminability values reached $d' = 0.5$ approximately 0.5 s after trial onset and
141 remained above this value throughout the trial duration, with peak $d' = 1.31 \pm 0.09$. The state axis defined
142 by attentional modulations remained stable throughout the duration of the trial (Supplementary Fig. 2d),
143 consistent with periods of high and low sustained attention that persisted across trials²¹. The anterior-
144 medial visual areas and the retrosplenial cortex contributed the most to large d' discriminability (Fig. 2g,
145 Supplementary Fig. 2d).

146 Together, these results showed that sensory inputs, movement-related activations, and
147 attentional signals were concurrently present in the posterior cortical regions, and could be separated by
148 the locaNMF tensor decomposition, permitting the identification of their characteristic spatial and
149 temporal signatures.

Choice signals

150 This approach also allowed us to identify choice-related signals. We adopted an operational definition of
151 choice as signals that correlated with animals' L/R decisions, independently of the stimulus and with
152 premotor signatures reflecting action selection⁷⁸. We considered trials in which the first detected wheel
153 rotation occurred at least half a second after stimulus onset. When occurring in the open loop, the
154 detected movement did not always coincide with the movement terminating the trial. However, we
155 confirmed that the direction of the first movement had a large and significant correlation with the trial
156 choice (85 ± 4 % agreement with movement directions), suggesting that the decision was made quickly
157 after the stimulus presentation (Supplementary Fig. 5c-d). We then aligned responses relative to
158 movement times and defined a state axis that linearly discriminated clockwise from counterclockwise
159 wheel rotations (hereafter left and right choice, respectively). LocaNMF projections onto this axis sharply
160 separated left from right choices (Fig. 3a), reaching peak separation values approximately 0.15 s after
161 movement detection (Fig. 3b; peak $d' = 1.5 \pm 0.1$) and with the choice axis showing two clearly stable
162 regions before and after movement onset (Fig. 3c). Area-specific d' values started to increase before
163 movement onset (Fig. 3d. Supplementary Fig. 7) from baseline, significantly so starting 300 ms before
164 movement onset ($p < 0.05$, paired t-test). We characterized pre-movement components using a piecewise
165 linear regression analysis (Fig. 3e) applied to d' curves to quantify the slope of the fit before the movement
166 and the time of the slope change (Fig. 3f-g). We found a consistent trend for positive pre-movement slopes
167 (ramping) and pre-movement slope change times (slope = 0.19 ± 0.06 d'/s , $p = 0.007$, t-test; time of slope
168 change = -0.06 ± 0.02 s, $p = 0.014$, t-test), providing evidence for temporally and spatially distributed pre-
169 movement choice components across these regions.

170 We reasoned that although evidence accumulation might not be a relevant factor in our task, a
171 decision variable⁷⁹—reflected in the time-varying d' values—would still retain its sensitivity to task
172 difficulty. Indeed, we found that in high-attention states, d' curves reflected stronger choice separation in
173 easy trials than in difficult trials (Fig. 3h; peak $d' = 1.4 \pm 0.1$ and 1.3 ± 0.1 , respectively; paired t-test, $p =$
174 0.003). In low-attention states, a similar trend was observed, but the difference was not significant (paired

175 t-test, $p = 0.4$). The dependence of d' values on task difficulty in high-attention states revealed that
176 attention enabled a modulation of the decisional process in proportion to trial-to-trial difficulty changes.
177 An analysis of wheel velocities confirmed d' modulations did not simply reflect a difficulty-dependent
178 change in motor control (Supplementary Fig. 8a-b). Choice axes independently defined in low- and high-
179 attention states were highly correlated (Pearson's $r = 0.72 \pm 0.03$), indicating they reflected a congruent
180 underlying decisional process. Finally, to examine whether the spatial integration embedded in the
181 locaNMF decomposition was critical for the detection of choice signals, we repeated the d' analysis,
182 defining state axes based on the activity of individual pixels independently from each other. Both before
183 and after movement onset, this analysis was unable to separate left and right choice trajectories
184 (Supplementary Fig. 8c), in agreement with recent reports relying on a similar independent-pixel
185 analysis^{26,54,55}.

186 Together, these results indicated that choice signals, sparsely distributed in the posterior cortex
187 could be detected through spatial integration; they defined a subspace for left and right trajectories, with
188 a stable representation across states of attention, but with attention enabling difficulty-dependent
189 modulations of response trajectories (Fig. 3j).

Distinct spatial and temporal characteristics of choice signals

190 Distinct signatures of choice signals were evident in the pairwise angular distance between state axes (Fig.
191 4a). Overall, angles between state axes were greater than 44° , with the choice axis being near-orthogonal
192 to the sensory-, movement-, and attention-related axis. Sensory and movement components had large
193 angles ($69 \pm 2^\circ$, mean + s.e.), and the smallest angles were observed between the movement and
194 attentional axes ($44 \pm 4^\circ$). In time, choice axes computed separately before (-0.1 s) and after (0.3 s)
195 movement onset were relatively stable in the pre- and post-movement periods and orthogonal to each
196 other ($81 \pm 3^\circ$, with 79° – 89° the expected 95% CI for independent axes; Methods; Fig. 3c, Fig. 4a). The
197 angle between movement axes, similarly computed across time windows, was also stable with angles of
198 approximately 70° ($69 \pm 5^\circ$; Fig. 4A, Supplementary Fig. 2b). Hierarchical clustering analysis on the angular
199 distances (Fig. 4b) highlighted that choice axes pre- and post-movement clustered together and were the
200 most dissimilar to the other state axes.

201 Irrespective of the time period, choice was always orthogonal to the movement axes (Fig. 4c
202 inset). When transitioning from the pre- to the post-movement period, d' values never collapsed to zero
203 (Fig. 3b), suggesting a rotation of the choice axis that preserved the orthogonality between choice and
204 movement axes. This can be understood as a rotating state axis for choice in a multi-dimensional choice
205 sub-space, that remained orthogonal to a similarly defined movement subspace (Fig. 4c).

206 In addition to these overall representational differences, choice signals also had distinct spatial
207 characteristics relative to other variables. We defined a spatial distribution index (SDI) that captured
208 whether several or only a few areas contributed prominently to the d' discriminability and found that
209 choice had the largest SDI values (more distributed, $30 \pm 4\%$) compared with sensory, movement, and
210 attentional signals (approximately 10%) (Fig. 4d). To further examine the area-specific contributions to
211 choice signals, we divided higher visual areas into three main groups—ventral (L), dorsal (PM, AM), and

212 parietal (A, RL, AL)⁶⁹—and separately analyzed somatosensory (SSt, SSb) and retrosplenial (RS) regions. V1
213 contributed an overall uniform d' value to all separations (Supplementary Fig. 2a-b); hence, we did not
214 include it in this analysis of relative differences. We then computed d' values using only the locaNMF
215 components that originated from these grouped areas and did this for all variables: visual, movement,
216 choice, and attention. This resulted in a five-dimensional (5D: ventral, dorsal, parietal, somatosensory,
217 and retrosplenial) space, where the coordinates of a variable reflected the distinct contribution of the
218 grouped areas to the d' separability of that variable. When examining discriminability power in 2-D
219 projections of this 5-D space (Fig. 4e), we could identify area-specific contributions. Stimulus and choice
220 post movement onset presented the largest contribution in the ventral stream (stimulus, $d' = 1.11 \pm 0.12$;
221 choice post $d' = 0.87 \pm 0.13$). These contributions were significantly larger than those in parietal and dorsal
222 stream areas (ventral vs parietal: $p = 0.012$ and $p = 0.019$ for stimulus and choice; ventral vs dorsal: $p =$
223 0.011 and $p = 0.043$; paired t-test). For the discriminability of attentional states, the parietal and dorsal
224 stream regions had larger contributions than ventral stream regions (high vs low sustained attention,
225 ventral vs parietal: $p = 0.015$; ventral vs dorsal: $p = 0.008$; paired t-test). Dorsal and parietal areas
226 contributed the most to the discriminability of movement variables, with the parietal areas having the
227 largest d' for wheel movements (dorsal vs parietal: $p = 0.001$; ventral vs parietal, $p = 0.014$; paired t-test).
228 Retrosplenial and somatosensory areas contributed similarly to the discriminability of choice and
229 movements, with d' values generally correlated across all variables ($r = 0.79$; 95% confidence intervals
230 $[0.64, 0.87]$, p -value $< 10^{-11}$, for d' correlations between somatosensory and retrosplenial areas across
231 animals).

232 In summary, distributed choice signals were distinct from sensory, movement, and attentional
233 components, dominantly in ventral-stream visual areas and modulated by task difficulty and attention,
234 suggesting that they might reflect the decision-making computations associated with the discrimination
235 task.

RNN modeling of decision dynamics

236 To examine this possibility, we used RNNs as implementation-level, mechanistic models of the decision-
237 making process. Building on previous work showing that RNNs can capture decision-making computations
238 associated with 2AFC discrimination tasks^{80,81}, we examined the dynamics of RNNs trained according to
239 the invariance for absolute orientations built into our task—and learned by the animals. Furthermore,
240 rather than using the optimal task solution, we trained RNNs with the trial-to-trial choices of the animals,
241 and introduced variability in attention states (Fig. 5a). Using the animals' choices rather than the task rule
242 created numerous “contradictory” examples, where the input evidence for a left or right choice was non-
243 deterministically associated with left or right output decisions, even in the easiest trials (e.g., non-zero
244 lapse rate). As a result, although RNNs were trained to produce L/R binary choices, they learned analogue
245 outputs that followed a psychometric probability function (Fig. 5a). Furthermore, output amplitudes
246 depended only on task difficulty, reflecting a learned invariance for absolute orientations. Context-
247 dependent attention modulations (introduced as an additional binary input) modified output probabilities
248 and created shallower or steeper psychometric curves in low or high attention states, respectively (Fig.

249 5a). Although the model was trained only with a subset of 13 difficulties and two attention states, it was
250 able to generalize to any difficulty level and range of attention within the trained boundaries (Fig. 5b). We
251 then analyzed the internal dynamics of the network by computing choice and attention axes from RNNs
252 unit responses, as we did for the neural data with locaNMF components. In the RNNs the choice axis
253 identified a decision variable that represented L/R decisions as separate trajectories in a low-dimensional
254 embedding space (Fig. 5c,d). Furthermore, the separation between L/R trajectories was modulated by
255 task difficulty, with larger separations in easy trials. This separation did not depend on absolute
256 orientations, as expected from the RNN having learned this invariance. The choice axis was stable across
257 levels of difficulty (Fig. 5e). Attentional modulations maintained an invariant representational geometry
258 of the decision variable across the embedding space (Fig. 5d-h). This was consistent with observations of
259 the neural data, where choice and attention axes were near-orthogonal with each other (Fig. 4a). In
260 summary, the representational similarity between the RNN and neural dynamics, together with the lack
261 of neural information provided to the network, indicated that the contextually modulated choice signals
262 observed in locaNMF components indeed represented the decision-making computations underlying the
263 orientation discrimination task.

Discussion

264 In this study, we used a complex visually guided task to isolate choice signals broadly distributed in the
265 posterior cortex and near-orthogonal to sensory-, movement-, and attention-related variables. We
266 showed that choice signals were prominent in ventral-stream visual areas. Choice signals defined left-right
267 trajectories in a low-dimensional activity space that were modulated by task difficulty, with this
268 modulation enabled contextually by the attention state of the animal. Using RNNs trained on the animals'
269 choices, we showed that the representational dynamics of choice signals were consistent with the
270 decision-making computations underlying the behavioral task. These results suggest a multiplexed
271 representation of variables in the posterior cortex, with a widespread distribution of decisional
272 information, possibly mediating probabilistic inference computations; for instance, information about the
273 ongoing decision-making process could be used for perceptual inference with unreliable sensory
274 stimuli^{82,83} and to influence sensory-to-decision signal transformations that inform future action plans.
275 Collectively, our results highlight task and analytical constraints for the detection of choice signals in the
276 mouse posterior cortex, aligning decision-making research in mice during visually guided behaviors with
277 primate studies.

Methodological relevance

278 We achieved these results by combining two powerful methods for the analysis of population responses:
279 locaNMF and activity-mode analysis. LocaNMF reduced the dimensionality of the neural data while
280 retaining spatial information, that would have been lost with traditional dimensionality reduction
281 methods (e.g., PCA). Furthermore, the state space representation allowed further reduction of
282 dimensionality by aligning the dynamics along task and decision-relevant dimensions. This latter step took

283 place within an interpretable linear framework, where the angle between the state axes as well as d'
284 values could be directly linked to the linear discriminability of the underlying variables.

285 The imaging methodology and data analysis used in this study facilitated the identification of
286 distributed choice signals encoded by sparse populations of cells⁸⁴. Indeed, sparse encoding in multi-
287 region networks would make choice signals hard to detect with methods that examine decision
288 information independently at each cortical location, whether because of the use of a single electrode (or
289 multi-contact electrode shank) or because of imaging data analysis focused on individual locations (pixels)
290 independent from each other. We confirmed this observation by reanalyzing our data at the single pixel
291 level and failing to detect choice information both before and after movement onset. This result may
292 explain why some recent mouse studies have failed to detect choice signals in posterior cortices during
293 similar visually guided tasks^{26,53–55}. Another contributing factor could have been task complexity. In our
294 task, mice were asked to make a relative comparison between stimulus orientations, a difficult task even
295 for primates^{63,85}, whereas other studies used simpler visual detection²⁶ or contrast discrimination tasks⁵⁴.
296 More complex perceptual decisions engage more spatially distributed networks³⁰; therefore, the
297 complexity of our task might have facilitated the emergence of choice signals in these posterior cortical
298 regions.

Feedback origin of choice signal

299 Choice signals emerged after stimulus onset, were broadly distributed in the posterior cortex, and could
300 be significantly detected as early in the visual hierarchy as in V1, suggesting feedback activations from
301 areas causally involved in the decision-making process. Other nonsensory signals identified in our
302 recordings, (e.g. related to body and eye movements), could also result from feedback activations. Indeed,
303 feedback signals to the posterior cortex have been extensively documented in the literature, in association
304 with a great diversity of underlying variables and computations, including attentional modulations⁸⁶,
305 movement-associated responses²², sensory context⁸⁷, and predictive coding⁸⁸.

Choice signals have distinctive spatial and temporal signatures

306 The properties of the choice signals met several criteria that are characteristic of a decision variable. Their
307 pre-movement components suggested that they did not simply reflect the execution of a motor plan or
308 an “unsigned” pre-motor preparatory state⁸⁹. Choice signals did not simply reflect bottom-up, stimulus-
309 related information that correlated with the decision process because, given the task design, the
310 contralateral stimulus orientation was uninformative for L/R decisions⁶³, furthermore, at the mesoscale
311 resolution used in this study, we showed orientations were not decodable from the neural signal⁹⁰. In
312 addition, choice signals were modulated by task difficulty, with the strength of the modulation dependent
313 on the attentive state of the animal.

314 Choice signals could be separated from movements. The cortical localization of movement
315 components was prominent in dorsal-stream regions, consistent with previous reports²¹. Choice signals
316 were instead localized in the retrosplenial cortex and in the visual cortex, mostly in ventral stream regions,
317 along the so-called “what” visual pathway⁹¹. This was consistent with the task requirements: mice had to

318 evaluate the orientation “content” of both stimuli and make relative orientation comparisons. Absolute
319 orientations were uninformative, as were the locations of the stimuli, which were unchanged across trials;
320 thus, in contrast to the “where” type of information, which is supposedly associated with dorsal stream
321 regions, solving the task relied on “what” information in ventral stream areas.

322 We also verified that ventral stream responses were not linked to eye movements
323 (Supplementary Fig. 9a), which typically followed whole-body movements²¹, or to stimulus movement
324 (Supplementary Fig. 9b) However, signals detected in ventral areas may still be associated with motor-
325 related components that also carry choice-relevant information⁹².

326 Attention-mediated modulations were orthogonal to the subspace defined by choice variables, with
327 the choice axis remaining significantly autocorrelated across time irrespective of attentional state. This
328 can be described as an isomorphic transformation in the embedding space of the decision variable, where
329 the subspace defined by the L/R trajectories is *shifted* without deforming the representational geometry.
330 The modulation of the decision variable with task difficulty was clear in high-attention trials, but not
331 significant in low-attention states. This might reflect an actual dependence of the decision-making process
332 on attention, given that mice might commit to a difficulty-independent heuristic strategy in low-attention
333 states⁶³.

334 The analysis of angles between state axes highlighted a large angular separation between variables,
335 with choice and movements remaining orthogonal to each other before and after movement onset.
336 However, movement onset correlated with a 90° rotation in the choice axis while retaining orthogonality
337 with movements. This phenomenon can be interpreted as movement signals affecting the multi-area
338 dynamics as an endogenous “contextual” input triggering a rotational dynamic in a multi-dimensional
339 choice space^{81,93}. A similar rotational dynamic was observed for movements signals in a movement space,
340 but the subspaces defined by choice and movement rotations remained orthogonal to each other. The
341 large angular difference between pre- and post-movement axes indicated distinct preparatory and
342 movement response signatures in the posterior cortex, possibly reflecting a similar distinction in anterior
343 motor regions^{89,94}. Movement signals potently increased neuronal activity across multiple posterior
344 regions^{20,21}. These large activations occupy the main dimensions of variability²³, effectively “forcing” a
345 representation shift in other variables while keeping them separate, that is, under orthogonality
346 constraints. Cellular-level simultaneous recordings from motor areas and posterior cortical regions may
347 provide further evidence for this interpretation in future studies.

348 Sensory and movement axes had the smallest separation. This latter observation agreed with previous
349 reports both at the local scale of small neuronal assemblies²³ and at the mesoscale²¹, indicating a
350 covariability axis between these variables. Similarly, the smaller angles observed between the movement
351 axis and the attentional axis agreed with a recent report showing that attention enhances distinctive
352 spatial features in movement-related activations across these cortical regions²¹. However, even after axes
353 orthogonalization, decoding attentional and movement information was still possible.

RNN implementation and mechanistic insights

354 Recurrent state-space models, including RNNs, have been previously used in mechanistic investigations
355 of decision-making processes^{80,81}. Moreover, representational similarity analysis of the state-space of
356 RNNs and neural responses has been successfully used to infer underlying computations⁸¹. Here, we
357 adopted a similar approach, but with three main distinguishing features. First, we trained the network
358 with the animals' decisions, rather than the task rule. This constituted a relevant departure from previous
359 research, which added noise to fully deterministic RNNs to capture logistic behavioral tuning functions^{80,95}.
360 Instead, we trained the network with "contradictory" information, such as that involved in the
361 inconsistent trial-to-trial animals' decisions, thus exposing the network to the biases and heuristics of the
362 animals. This allowed the network to capture the probabilistic choice behavior of the animal, agnostically
363 relative to the causes underlying the animals' trial-to-trial variability. Training with the animal choices was
364 akin to training with label noise, for which many deep learning algorithms are robust⁹⁶. The RNN outputs
365 effectively implemented two dynamic *accumulators* providing time-dependent scores for L/R choices,
366 with the difference between the scores being proportional to the psychometric function. This result was
367 probably related to the mathematical observation that if L/R choices were determined by two
368 accumulators (for the left or right evidence, respectively), the log-likelihood ratio of the conditional
369 probabilities for a given choice, given the state of the accumulators, can be shown to be proportional to
370 the psychometric (logistic) function^{97,98}. The temporal dynamics of the RNN enabled a representational
371 comparison with the time-evolving neural trajectories, but it was not intended as a mechanistic descriptor
372 of a decision time. The second novelty was that we trained the RNN to learn an invariance regarding
373 absolute orientations, which were uninformative for the task choice and that was readily learned by the
374 network. Finally, the third novelty concerned attentional modulations. As observed in the neural data, the
375 added attentional input to the RNN caused an isomorphic shift of the decision-making manifold, which
376 retained the geometry of the decision variable. Geometry-preserving isomorphic shifts in low-dimensional
377 embedding spaces, might reflect a general "decorrelation" principle for variables that are concurrently
378 represented across overlapping cortical networks⁹⁹. These results confirmed that, mechanistically, the
379 representational dynamic of choice signals reflected the decision-making computations underlying the
380 animals' psychophysical behaviors.

Limitations and open questions

381 Our results raise several questions to be addressed in future studies; for instance, whether the broad
382 distribution of choice signals mirrored equally broad spiking activations is still unclear. Regarding
383 anatomical considerations, feedback signals are known to preferentially target deep layers (five and six)
384 and layer one¹⁰⁰. Considering that our imaging microscope focused on superficial cortical layers and that
385 GCaMP was expressed across the cortex, choice signals might reflect long-range axon-terminal activations
386 and /or depolarizations in apical dendritic trees rather than somatic firing¹⁰¹. Concurrent imaging and
387 electrophysiological recordings across layers would clarify this point.

388 Our study relied on correlative measures; therefore, loss- and gain-of-function perturbative
389 experiments will be necessary to establish causality. Of particular interest would be the inactivation of

390 lateral visual areas in view of the observed ventral-stream prominence. Furthermore, patterned
391 optogenetic methodologies with single-cell resolution might enable the stimulation of the individual
392 neurons that most significantly carry choice-relevant information in these regions.

393 In summary, broadly distributed feedback decision signals, with a representational dynamic
394 consistent with decision-making computations underlying a visually guided perceptual task, represent a
395 computational substrate capable of modulating early sensory processing and sensory to decision
396 transformations. These modulations, however, depend on the underlying decision-making process and
397 might involve probabilistic-inference computations in changeable agent-environment interactions¹⁰².

Methods

398 Experimental procedures

399 Details of the experimental procedures (surgeries, behavioral training, recordings of body and eye
400 movements, imaging methods, and pre-processing of fluorescence data) have been described in
401 Abdolrahmani and collaborators²¹. We summarize them here in brief.

402 Surgeries

403 All surgical and experimental procedures were approved by the Support Unit for Animal Resources
404 Development of RIKEN CBS. The transgenic mice used in this work were Thy1-GCaMP6f mice (n = 7). For
405 all reported results, the number of valid sessions per animal ranged from 11 to 35, with a minimum and
406 maximum number of trials per animal of 2,000 to 5,000. The Animals were implanted with cranial posts
407 for head fixation and a round chamber consisting of two overlapping glass coverslips (6mm diameter) for
408 optical access to neural recordings.

409 Behavioral training

410 Animals were trained on a 2AFC orientation discrimination task following the iterative protocol presented
411 in⁶³. The final stage of the task consisted of two oriented Gabor patches shown to the left and right side
412 of a screen positioned in front of the animals at $\pm 35^\circ$ eccentricity relative to the body's midline. Mice had
413 to report which of the two stimuli matched a target orientation (vertical, n = 5; horizontal, n = 2). The
414 smallest orientation difference was 9° except for one animal where it was 3° . The largest difference—the
415 easiest discrimination—was $\pm 90^\circ$. Animals signaled their choice by rotating a rubber wheel with their
416 front paws, which shifted stimuli horizontally on the screen. Every trial consisted of an open-loop period
417 (OL: 1.5 s) starting after stimulus onset, during which wheel rotations did not produce any stimulus
418 movement, and a closed-loop period (CL) starting after the end of the OL and lasting 0–10 s, followed by
419 an inter-trial interval (ITI: 3–5 s randomized). For a response to be correct, the target stimulus had to be
420 shifted to the center of the screen, which led to the animal being rewarded with 4 μ L of water. Incorrect
421 responses were discouraged with a prolonged (10 s) inter-trial interval and a flickering checkerboard
422 stimulus (2 Hz). If no response was made within 10 s (time-out trials), neither reward nor discouragement
423 was given. Animals were imaged after exceeding a performance threshold of 75 % correct rate for 5–10
424 consecutive sessions. To work with a coherent behavioral dataset, we excluded sessions with exceedingly
425 large fractions for time-outs (≥ 20 %) or with average performance below 60 %. We recorded cortical
426 responses, wheel rotations, and eye/pupil videos from a 1 s pre-stimulus period until the end of the trial.

427 Saccades, pupil area, and body movements

428 We monitored the contralateral eye using a CMOS camera. Automatic tracking of the pupil position was
429 done with custom software (Matlab, Mathworks®). We confirmed the accuracy of pupil tracking by
430 visually observing hundreds of trials. Saccade detection was achieved by applying an adaptive elliptic
431 thresholding algorithm to saccade velocities (as detailed in²¹). We discarded saccades that lasted ≤ 60
432 ms and were smaller than 1.5° . We extracted the time, magnitude, duration, velocity, start and landing
433 positions of each saccade. We calculated the average pupil area for each imaging session by averaging

434 area values across all trials within the session. Pupil area amplitudes in every trial were z-scored,
435 centering values relative to the session mean.

436 Wheel detection

437 We recorded wheel rotations with a rotary encoder attached to the wheel and flagged as potential wheel
438 movements the time points when the velocity had a zero-crossing (i.e., a sign change) and deviated from
439 zero above a fixed threshold (20°).

440 Imaging

441 Mice were placed under a dual cage THT macroscope (Brainvision Inc.) for wide-field imaging in tandem-
442 lens epifluorescence configuration using two AF NIKKOR 50 mm f/1.4D lenses. We imaged GCaMP6f
443 fluorescent signals using continuous illumination and a CMOS camera (PCO Edge 5.5) with acquisition
444 speeds of either 30 or 50 fps. Illumination consisted of a 465 nm centered LED (LEX-2, Brainvision Inc.), a
445 475 nm bandpass filter (Edmund Optics BP 475 x 25 nm OD4 ϕ = 50 mm) and two dichroic mirrors with
446 506 nm and 458 nm cutoff frequencies, respectively (Semrock FF506-Di03 50 x 70 mm, FF458-DFi02 50 x
447 70 mm). Fluorescence light path travelled through the two dichroic mirrors (458 and 506 nm respectively)
448 and a 525 nm bandpass filter (Edmund Optics, BP 525 x 25 nm OD4 ϕ = 50mm).

449 Pre-processing of fluorescence data

450 GCaMP data was registered automatically using Fourier-based subpixel registration¹⁰³. To compute
451 relative fluorescence responses, we calculated a grand-average scalar $F_0^{i,j} = \langle I_{x,y,t}^{i,j} \rangle_{x,y,t}$, with
452 $I_{x,y,t}^{i,j}$ representing the XYT image tensor in trial i , session j . We then used this scalar to normalize the raw
453 data tensor $F_{x,y,t}^{i,j} = (I_{x,y,t}^{i,j} - F_0^{i,j}) / F_0^{i,j}$. The data for each trial were then band-pass filtered (0.1 to 8
454 Hz). Each tensor was compressed with spatial binning (130 × 130 μm^2 with 50% overlap). Trial data
455 recorded at 50 fps was further downsampled to 30 fps.

456 Hemodynamic correction of fluorescence data

457 In recordings to control for the hemodynamic signal, we followed a previously reported methodology^{73,104}.
458 Briefly, cortical tissue was illuminated at 60 Hz with 15 ms exposure by interleaving shutter-controlled
459 blue and violet LEDs. Blue light path consisted of a 465 nm centered LED (LEX-2, Brainvision Inc.), a 475
460 nm bandpass filter (Edmund Optics BP 475 x 25 nm OD4 ϕ = 50 mm) and two dichroic mirrors with 506
461 and 458 nm cutoff frequencies, respectively (Semrock FF506-Di03 50 x 70 mm, FF458-DFi02 50 x 70 mm).
462 The violet path consisted of a 405 nm centered LED (Thorlabs M405L2 and LEED1B driver), a 425 nm
463 bandpass filter (Edmund Optics BP 425 x 25 mm OD4 ϕ = 25 mm), a collimator (Thorlabs COP5-A) and
464 joined the blue LED path at the second dichroic mirror. Fluorescence light path travelled through the two
465 dichroic mirrors (458 and 506 nm respectively) and a 525 nm bandpass filter (Edmund Optics, BP 525 x 25
466 nm OD4 ϕ = 50 mm) and was captured with a PCO Edge 5.5 CMOS camera with cameralink interface.
467 Camera acquisition was synchronized to the LED illumination via a custom Arduino-controlled software.
468 Frame exposure lasted 12 ms starting 2 ms after opening each LED shutter.

469 Continuously acquired imaging data was then split into blue and violet channels and registered
470 independently to account for motion artifacts. For every pixel blue and violet data was independently
471 transformed to a relative fluorescence signal, $\frac{\Delta F}{F} = (F - aF - b)/b$, where F is the original data and a
472 and b coefficients are obtained by linear fitting each timeseries, i.e., $F(t) \sim at - b$. Afterwards, for each
473 pixel, violet $\frac{\Delta F}{F}$ signal was low-pass filtered (6th order IIR filter with cutoff at 5 Hz) and linearly fitted to the
474 blue $\frac{\Delta F}{F}$ signal: the hemodynamic-corrected $\frac{\Delta F}{F}$ signal was obtained as $\frac{\Delta F}{F} corr = \frac{\Delta F}{F} blue -$
475 $(c \frac{\Delta F}{F} violet + d)$, where c and d are the coefficients from linearly fitting the low-pass filtered $\frac{\Delta F}{F} violet$
476 to the $\frac{\Delta F}{F} blue$ signal, i.e., $\frac{\Delta F}{F} blue(t) \sim c \frac{\Delta F}{F} violet(t) - d$. Finally, $\frac{\Delta F}{F} corr$ was low-pass filtered (6th order
477 IIR filter with cutoff at 8 Hz) and spatially downsampled such that every pixel measured 50 x 50 μm^2 .

478 Retinotopies

479 We used a standard frequency-based method (Kalatsky and Stryker, Neuron 2003) with slowly moving
480 horizontal and vertical flickering bars and corrections for spherical projections¹⁰⁵. Visual area
481 segmentation was performed based on azimuth and elevation gradient inversions. Retinotopic maps were
482 derived under light anesthesia (Isoflurane) with the animal midline pointing to the right edge of the
483 monitor (IIYAMA Prolite LE4041UHS 40") and the animal's left eye at a distance of 35 cm from the center
484 of the screen.

485 Alignment to the Allen Mouse Brain Common Coordinate Framework

486 Imaging data from each animal was aligned to the Allen Mouse Brain Common Coordinate Framework
487 (CCF) following the approach described by Waters¹⁰⁶. In brief, we extracted the centroids of areas V1, RL
488 and PM, using them to create a triangle that we aligned to the one from the Allen CCF. We did so by first
489 making the V1 vertices coincide and then rotated and scaled the triangle to minimize the distance
490 between the other vertices while maintaining the original angles.

491 Data processing

492 LocaNMF

493 LocaNMF analysis was conducted following the methods described by Saxena⁶⁴. Imaging data across all
494 trials and sessions was first concatenated and its dimensionality reduced using singular-value
495 decomposition (SVD) up to 99 % of the original variance. LocaNMF was initialized using 10 regions based
496 on the Allen CCF and centered on V1 (VISp), PM (VISpm), AM (VISam), A (VISa), SSt (SSp-tr), RL (VISrl), SSb
497 (SSp-bfd), AL (VISal), L (VISl and VISli), and RS (RSPagl and RSPd) (Supplementary Fig. 1), with regions
498 extending beyond retinotopically-defined area boundaries. For each region, a spatial mask was created
499 by setting a distance $D = 1$ within the region boundaries and an exponential decrease (to zero) for pixels
500 outside the boundary. The localization penalty for each pixel was 1-D (Supplementary Fig. 1a). LocaNMF
501 rank line search was run for these 10 regions with a localization threshold of 75 % and total explained
502 variance of 99 %, resulting on average in approximately 200 components per animal. After decomposition,
503 temporal components were separated back into the original trial structure. More formally, LocaNMF
504 produced a decomposition tensor $F_{x,y,t}^i \sim \sum_k A_{x,y,k} C_{k,t}^i$ for trial i , where $A_{x,y,k}$ is the spatial part of

505 component k , and $C_{k,t}^i$ is its temporal part. The spatial parts of the components were significantly localized
506 and could be mapped onto the original seeding region. The temporal component captured the unique
507 trial-to-trial variability, and all subsequent analyses in the time domain were conducted using only the
508 temporal $C_{k,t}^i$ of locaNMF components. Total explained variance (EV) of the decomposition was computed
509 by projecting one component at a time across the whole time series and measuring the relative explained
510 variance across pixels with the original recording.

511 State Axis definition

512 We defined a state axis as a one-dimensional projection of locaNMF temporal components $\mathbf{C}(t)$ that
513 maximized the weighted distance between the trajectories of two trial groups **A** and **B** (bold letters
514 indicate vectors). For each group, we defined trial-averaged trajectories $\langle \mathbf{A}(t) \rangle$ and $\langle \mathbf{B}(t) \rangle$ and defined

515 $\mathbf{S}(t) = \left\| \frac{\langle \mathbf{A}(t) \rangle - \langle \mathbf{B}(t) \rangle}{\sigma_{AB}(t)} \right\|$, where $\sigma_{AB}(t) = \sqrt{\frac{1}{2}(\sigma_{A(t)}^2 + \sigma_{B(t)}^2)}$ is the pooled standard deviation between

516 the two groups. State axis projections for the i -th trial were then obtained by the dot product $P^i(t) =$
517 $\mathbf{S}(t) \cdot \mathbf{C}^i(t)$, where $\mathbf{C}^i(t)$ are the temporal locaNMF components of trial i . Discriminability between the

518 original A and B groups was then computed as $d' = \frac{\langle P_A^i(t) \rangle - \langle P_B^i(t) \rangle}{\sigma_{P_A P_B}(t)}$, that is the difference between the

519 averaged projections of groups A and B, divided by their pooled standard deviation. To validate state axes
520 projections and discriminability we performed five-fold cross validation: state axes were defined using
521 only 20% of the trials of each group and projections and d' were computed on the remaining trials. To
522 compute and validate the state axes, both groups **A** and **B** always had the same number of trials (i.e., the
523 number of trials in the smallest group and a random set of the same size from the other group).

524 State axes stability

525 To assess the stability of state axes, we computed instantaneous state axes $\mathbf{S}(t)$ using a “backward” three-
526 frame averaging window (around 100 ms) and then computed its temporal autocorrelation $C(\mathbf{S}(t), \mathbf{S}(t'))$.

527 For sensory, movement, and sustained attention state axes we chose the time-independent state axes
528 $\mathbf{S} \equiv \mathbf{S}(t^*)$, where t^* was chosen from the largest stability cluster (represented by a gray bar in the
529 respective figures). For the state axis of choice, we used the original $\mathbf{S}(t)$ to monitor when choice
530 information first appeared and whether its signature was unique.

531 Task-related state axes

532 **Stimulus:** For stimulus state-vectors, we used for the first group (**A**) all the trials in the time interval (-0.5
533 to +0.5 s) centered on the stimulus onset. For group **B**, since the stimulus was present in all trials, we used
534 the same trials in the preceding time interval (-1 to 0 s) as the no stimulus condition.

535 **Contralateral stimulus:** We used trials with the left stimulus horizontal as group **A** and the trials with the
536 left stimulus vertical as group **B** (Supplementary Fig. 3).

537 **Wheel movement:** Group **A** consisted of trials for which the first movement after stimulus presentation
538 occurred at least 0.5 s after stimulus onset and without any saccade detected in the previous 0.5 s. These
539 trials were aligned to the detected movement onset. Group **B** consisted of trials with no movement

540 detected during the first 5 s after stimulus onset. These trials were aligned with respect to a frame picked
541 at random within the same time interval.

542 **Saccades:** Akin to the definition of wheel movements, Group **A** consisted of trials for which a saccade
543 after stimulus presentation occurred at least 0.5 s after stimulus onset and without any wheel movement
544 detected in the previous 0.5 s. These trials were aligned to the detected saccade time. Group **B** consisted
545 of trials with no saccade detected during the first 5 s after stimulus onset. These trials were aligned with
546 respect to a frame picked at random within the same time interval.

547 **Sustained attention:** Sustained attention was measured by changes in pupil area during the trial. We
548 computed pupil area changes (pA) as the difference between the maximum pupil area after stimulus onset
549 and the average area 1 s before stimulus onset. We labeled as “high sustained attention” trials (group **A**)
550 those in the top 33rd percentile of the pA distribution and as “low sustained attention” trials (group **B**)
551 those in the bottom 33rd percentile. Groups **A** and **B** were always balanced by definition.

552 **Choice:** L/R choices in each trial were measured from the direction of the first movement after stimulus
553 onset. The state axis for group **A** was computed from right-choice trials and for group **B** using left-choice
554 trials. As for the detection of wheel movements, we restricted the analysis to trials in which the first
555 movement occurred at least 0.5 s after stimulus onset and with no saccades 0.5 s before the detected
556 movement. Trials were aligned to the time of movement detection.

557 State axes independence

558 To determine confidence intervals of the angle formed between independent state axes (Fig. 4c), we
559 proceeded as follows. For each animal, we picked at random one of the original state axis, and sampled
560 with repetitions from its components to generate 2000 surrogate state axis with matched dimensionality.
561 The angle between the original vector and each of the surrogates was computed, resulting in an angle
562 ranging from 79 ° to 89 ° (2.5 % and 97.5 % confidence intervals).

563 Area-specific state axes

564 We defined state axes for each of the 10 areas by only using the subset of locaNMF components $C_{k,t}^i$ that
565 originated from that area. This was akin to first projecting onto the subspace defined by the components
566 of a particular area, and then obtaining the associated state axis.

567 Piecewise linear fitting of d' curves

568 To fit the time-evolving d' curves to periods before and after movement onset, we performed two-slope
569 piecewise linear fitting using the Shape Language Modeling toolbox (MATLAB Central File Exchange, John
570 D’Errico, 2021; SLM—shape language modeling; <https://www.mathworks.com/matlabcentral/fileexchange/24443-slm-shape-language-modeling>). This method performs two linear fits in a fixed
571 interval with a single knot between them. We chose the interval -1 s before movement onset up to the
572 95th percentile of the peak post-movement response amplitude (typically occurring around 0.3 s after
573 movement onset). The position of the knot determined the slope change time.
574

575 Spatial-Distribution Index (SDI)

576 The SDI for a given state axis was computed as $SDI (\%) = \left(\frac{d'_{global}}{\max(d'_i)} - 1 \right) \cdot 100$ where d'_i refers to the
577 area- specific d' scores, and d'_{global} refers to the discriminability of the state axis.

578 Pixel-wise choice decoding

579 To compute choice-related d' values for individual pixels, we proceeded as follows. Using the same groups
580 of trials described in “Task-related state axes—choice”, at each pixel and time (relative to movement
581 onset) we computed the mean and variance of the dF/F distribution for each group. We then computed

582 d' with the usual formula as $d'^{i,j}(t) = \frac{\langle dF/F_A^{i,j}(t) \rangle - \langle dF/F_B^{i,j}(t) \rangle}{\sigma_{dF/F_A} dF/F(t)}$, where i, j denotes the i -th row and j -th

583 column of the original dataset. This calculation was restricted to the pixels that were common across all
584 animals (pixels at the edges of the imaging window were not present in all animals due to different
585 alignment transformations to the reference dataset).

586 RNN Model

587 The RNN consisted of a single RNN module with $N = 128$ neurons (ReLU activations), receiving 3 inputs
588 (left stimulus, right stimulus, and attention level) and producing a binary response as an output for left or
589 right choices (softmax activation).

590 Inputs: The input space consisted of a sequence of 25 frames. Stimulus orientations were mapped to the
591 range of -1 to $+1$ (corresponding to -90° to $+90^\circ$) and were presented after the first 10 frames. The
592 difficulty of a trial was encoded by the absolute difference between the two stimulus signals. Attention
593 was modeled as a constant binary signal (0 or 1), already present at the beginning of the trial. A small
594 noise (normally distributed with amplitude 0.01) was added to the input signals to improve the robustness
595 of the optimization, but it was irrelevant for the psychometric fitting.

596 Training: For training the network, we generated simulated animal responses by computing L/R choices,
597 following a psychometric curve of the form $P_{left}(\theta) = \frac{1}{1+e^{-\alpha\theta}}(1-\lambda) + \frac{\lambda}{2}$, where θ is the difference
598 between the two inputs, λ is the lapse rate, and α controls the slope. We used a constant $\lambda = 0.1$ and
599 $\alpha = 3/90$ for low attention and $\alpha = 10/90$ for high attention; that is, attention decreased the amount
600 of label noise during training. To train the network, we used 6,400 trials per difficulty level and chose 13
601 difficulty levels with angle differences uniformly distributed from -90° to $+90^\circ$. We trained the network
602 using a batch normalization layer and a custom loss function consisting of the categorical cross entropy at
603 the time of stimulus presentation and at the last frame. The output was a binary vector with three
604 components (L, R, N), representing left, right, and no choice conditions. At the time of stimulus
605 presentation, the vector was set to $(0,0,1)$ and at the trial end to $(1,0,0)$ or $(0,1,0)$. We included the
606 stimulus presentation time and no-choice condition in the loss function to prevent the output drifting
607 before stimulus presentation, following a procedure used by Mante (Mante et al., Nature 2013). Accuracy
608 during training was computed using the categorical accuracy at the end of the trial. The network was
609 implemented with TensorFlow 2.0 and trained using the Adam optimizer for 25 epochs with a batch size
610 of 640. Note that training the network with the animal choices made the network robust to overfitting.

611 We trained 10 different networks by generating new sets of inputs and randomly initializing the network
612 weights.

613 Analysis: We analyzed the output of the RNN in the same way as for the neural data, but we used the
614 time series of the $N = 128$ neurons instead of the locaNMF components to define choice and attention
615 state axes.

References

- 616 1. Musall, S., Urai, A. E., Sussillo, D. & Churchland, A. K. Harnessing behavioral diversity to
617 understand neural computations for cognition. *Curr. Opin. Neurobiol.* **58**, 229–238 (2019).
- 618 2. Hausmann, S. B., Vargas, A. M., Mathis, A. & Mathis, M. W. Measuring and modeling the motor
619 system with machine learning. *Current Opinion in Neurobiology* **70**, 11–23 (2021).
- 620 3. Perich, M. G. & Rajan, K. Rethinking brain-wide interactions through multi-region ‘network of
621 networks’ models. *Current Opinion in Neurobiology* vol. 65 146–151 (2020).
- 622 4. Latimer, K. W. & Huk, A. C. Superior colliculus activates new perspectives on decision-making.
623 *Nature Neuroscience* 1–3 (2021) doi:10.1038/s41593-021-00885-7.
- 624 5. Rigotti, M. *et al.* The importance of mixed selectivity in complex cognitive tasks. *Nature* **497**, 585–
625 590 (2013).
- 626 6. Britten, K. H., Newsome, W. T., Shadlen, M. N., Celebrini, S. & Movshon, J. A. A relationship
627 between behavioral choice and the visual responses of neurons in macaque MT. *Vis. Neurosci.*
628 **13**, 87–100 (1996).
- 629 7. Crapse, T. B. & Basso, M. A. Insights into decision making using choice probability. *J.*
630 *Neurophysiol.* **114**, 3039–3049 (2015).
- 631 8. Lange, R. D. & Haefner, R. M. Characterizing and interpreting the influence of internal variables
632 on sensory activity. *Curr. Opin. Neurobiol.* **46**, 84–89 (2017).
- 633 9. Nienborg, H. & Cumming, B. G. Macaque V2 neurons, but not V1 neurons, show choice-related
634 activity. *J. of Neurosci.* **26**, 9567–9578 (2006).
- 635 10. Uka, T. & DeAngelis, G. C. Contribution of area MT to stereoscopic depth perception: Choice-
636 related response modulations reflect task strategy. *Neuron* **42**, 297–310 (2004).
- 637 11. Shadlen, M. N., Britten, K. H., Newsome, W. T. & Movshon, J. A. A computational analysis of the
638 relationship between neuronal and behavioral responses to visual motion. *J Neurosci* **16**, 1486–
639 1510 (1996).
- 640 12. Haefner, R. M., Gerwinn, S., Macke, J. H. & Bethge, M. Inferring decoding strategies from choice
641 probabilities in the presence of correlated variability. *Nat. Neurosci.* **16**, 235–242 (2013).
- 642 13. Macke, J. H. & Nienborg, H. Choice (-history) correlations in sensory cortex: cause or
643 consequence? *Curr. Opin. in Neurobiol.* vol. 58 148–154 (2019).
- 644 14. McCormick, D. A., McGinley, M. J. & Salkoff, D. B. Brain state dependent activity in the cortex and
645 thalamus. *Curr Opin Neurobiol* **31**, 133–140 (2015).
- 646 15. Miller, E. K. & Buschman, T. J. Cortical circuits for the control of attention. *Current Opinion in*
647 *Neurobiology* vol. 23 216–222 (2013).
- 648 16. Uka, T., Tanabe, S., Watanabe, M. & Fujita, I. Neural correlates of fine depth discrimination in
649 monkey inferior temporal cortex. *Journal of Neuroscience* **25**, 10796–10802 (2005).
- 650 17. Jasper, A. I., Tanabe, S. & Kohn, A. Predicting perceptual decisions using visual cortical population
651 responses and choice history. *The Journal of Neurosci.* **39**, 6714–6727 (2019).

- 652 18. Goris, R. L. T., Ziemba, C. M., Stine, G. M., Simoncelli, E. P. & Movshon, J. A. Dissociation of choice
653 formation and choice-correlated activity in macaque visual cortex. *J. Neurosci.* (2017)
654 doi:10.1523/JNEUROSCI.3331-16.2017.
- 655 19. Niell, C. M. & Scanziani, M. How Cortical Circuits Implement Cortical Computations: Mouse Visual
656 Cortex as a Model. *Annual Review of Neuroscience* **44**, annurev-neuro-102320-085825 (2021).
- 657 20. Musall, S., Kaufman, M. T., Juavinett, A. L., Gluf, S. & Churchland, A. K. Single-trial neural
658 dynamics are dominated by richly varied movements. *Nat. Neurosci.* **22**, 1677–1686 (2019).
- 659 21. Abdolrahmani, M., Lyamzin, D. R., Aoki, R. & Benucci, A. Attention separates sensory and motor
660 signals in the mouse visual cortex. *Cell Reports* **36**, 109377 (2021).
- 661 22. Parker, P. R. L., Brown, M. A., Smear, M. C. & Niell, C. M. Movement-related signals in sensory
662 areas: Roles in natural behavior. *Trends Neurosci.* **43**, 581–595 (2020).
- 663 23. Stringer, C. *et al.* Spontaneous behaviors drive multidimensional, brainwide activity. *Science* **364**,
664 255 (2019).
- 665 24. Krumin, M., Lee, J. J., Harris, K. D. & Carandini, M. Decision and navigation in mouse parietal
666 cortex. *eLife* **7**, (2018).
- 667 25. Kauvar, I. *et al.* Cortical Observation by Synchronous Multifocal Optical Sampling Reveals
668 Widespread Population Encoding of Actions. *Neuron* (2020) doi:10.1016/j.neuron.2020.04.023.
- 669 26. Salkoff, D. B., Zagha, E., McCarthy, E. & McCormick, D. A. Movement and Performance Explain
670 Widespread Cortical Activity in a Visual Detection Task. *Cerebral Cortex* **30**, 421–437 (2020).
- 671 27. Minderer, M., Brown, K. D. & Harvey, C. D. The spatial structure of neural encoding in mouse
672 posterior cortex during navigation. *Neuron* **102**, 232–248 (2019).
- 673 28. Koay, S. A., Thiberge, S. Y., Brody, C. D. & Tank, D. W. Amplitude modulations of cortical sensory
674 responses in pulsatile evidence accumulation. *eLife* **9**, 1–49 (2020).
- 675 29. Pinto, L. *et al.* An Accumulation-of-Evidence Task Using Visual Pulses for Mice Navigating in
676 Virtual Reality. *Front Behav Neurosci* **12**, 36 (2018).
- 677 30. Pinto, L. *et al.* Task-dependent changes in the large-scale dynamics and necessity of cortical
678 regions. *Neuron* **104**, 810–824 (2019).
- 679 31. Odoemene, O., Pisupati, S., Nguyen, H. & Churchland, A. K. Visual evidence accumulation guides
680 decision-making in unrestrained mice. *J Neurosci* (2018) doi:10.1523/JNEUROSCI.3478-17.2018.
- 681 32. Licata, A. M. *et al.* Posterior Parietal Cortex Guides Visual Decisions in Rats. *J Neurosci* **37**, 4954–
682 4966 (2017).
- 683 33. Scott, B. B. *et al.* Fronto-parietal Cortical Circuits Encode Accumulated Evidence with a Diversity
684 of Timescales. *Neuron* **95**, 385–398.e5 (2017).
- 685 34. Morcos, A. S. & Harvey, C. D. History-dependent variability in population dynamics during
686 evidence accumulation in cortex. *Nat Neurosci* (2016).
- 687 35. Erlich, J. C., Brunton, B. W., Duan, C. A., Hanks, T. D. & Brody, C. D. Distinct effects of prefrontal
688 and parietal cortex inactivations on an accumulation of evidence task in the rat. *Elife* **4**, (2015).

- 689 36. Hanks, T. D. *et al.* Distinct relationships of parietal and prefrontal cortices to evidence
690 accumulation. *Nature* (2015) doi:10.1038/nature14066.
- 691 37. Raposo, D., Kaufman, M. T. & Churchland, A. K. A category-free neural population supports
692 evolving demands during decision-making. *Nat Neurosci* **17**, 1784–1792 (2014).
- 693 38. Harvey, C. D., Coen, P. & Tank, D. W. Choice-specific sequences in parietal cortex during a virtual-
694 navigation decision task. *Nature* **484**, (2012).
- 695 39. Koay, S. A., Thiberge, S. Y., Brody, C. & Tank, D. W. Sequential and efficient neural-population
696 coding of complex task information. *bioRxiv* 801654 (2019) doi:10.1101/801654.
- 697 40. Gilad, A., Gallero-Salas, Y., Groos, D. & Helmchen, F. Behavioral Strategy Determines Frontal or
698 Posterior Location of Short-Term Memory in Neocortex. *Neuron* **99**, 814-828.e7 (2018).
- 699 41. Akrami, A., Kopec, C. D., Diamond, M. E. & Brody, C. D. Posterior parietal cortex represents
700 sensory history and mediates its effects on behaviour. *Nature* (2018) doi:10.1038/nature25510.
- 701 42. Driscoll, L. N., Pettit, N. L., Minderer, M., Chettih, S. N. & Harvey, C. D. Dynamic Reorganization of
702 Neuronal Activity Patterns in Parietal Cortex. *Cell* **170**, 986-999.e16 (2017).
- 703 43. Hwang, E. J., Dahlen, J. E., Mukundan, M. & Komiyama, T. History-based action selection bias in
704 posterior parietal cortex. *Nature Communications* **8**, (2017).
- 705 44. Chen, T.-W., Li, N., Daie, K. & Svoboda, K. A Map of Anticipatory Activity in Mouse Motor Cortex.
706 *Neuron* **94**, 866-879.e4 (2017).
- 707 45. Goard, M. J., Pho, G. N., Woodson, J. & Sur, M. Distinct roles of visual, parietal, and frontal motor
708 cortices in memory-guided sensorimotor decisions. *Elife* **5**, (2016).
- 709 46. Funamizu, A., Kuhn, B. & Doya, K. Neural substrate of dynamic Bayesian inference in the cerebral
710 cortex. *Nat Neurosci* **19**, 1682–1689 (2016).
- 711 47. Guo, Z. *et al.* Flow of cortical activity underlying a tactile decision in mice. *Neuron* **81**, 179–194
712 (2014).
- 713 48. Erlich, J. C., Bialek, M. & Brody, C. D. A cortical substrate for memory-guided orienting in the rat.
714 *Neuron* **72**, 330–343 (2011).
- 715 49. Poort, J. *et al.* Learning Enhances Sensory and Multiple Non-sensory Representations in Primary
716 Visual Cortex. *Neuron* (2015) doi:10.1016/j.neuron.2015.05.037.
- 717 50. Zhong, L. *et al.* Causal contributions of parietal cortex to perceptual decision-making during
718 stimulus categorization. *Nat Neurosci* (2019) doi:10.1038/s41593-019-0383-6.
- 719 51. Katz, L. N., Yates, J. L., Pillow, J. W. & Huk, A. C. Dissociated functional significance of decision-
720 related activity in the primate dorsal stream. *Nature* (2016) doi:10.1038/nature18617.
- 721 52. Chen, A., Gu, Y., Liu, S., DeAngelis, G. C. & Angelaki, D. E. Evidence for a Causal Contribution of
722 Macaque Vestibular, But Not Intraparietal, Cortex to Heading Perception. *Journal of Neuroscience*
723 **36**, 3789–3798 (2016).
- 724 53. Steinmetz, N. A., Zatka-Haas, P., Carandini, M. & Harris, K. D. Distributed coding of choice, action
725 and engagement across the mouse brain. *Nature* **576**, 266–273 (2019).

- 726 54. Zatka-Haas, P., Steinmetz, N. A., Carandini, M. & Harris, K. D. Sensory coding and causal impact of
727 mouse cortex in a visual decision. *bioRxiv* 501627 (2021) doi:10.1101/501627.
- 728 55. Lee, J. J., Krumin, M., Harris, K. D. & Carandini, M. Task specificity in mouse parietal cortex.
729 *bioRxiv* 2020.12.18.423543 (2020) doi:10.1101/2020.12.18.423543.
- 730 56. Krishna, A., Tanabe, S. & Kohn, A. Decision Signals in the Local Field Potentials of Early and Mid-
731 Level Macaque Visual Cortex. *Cerebral Cortex* **31**, 169–183 (2021).
- 732 57. Quinn, K. R., Seillier, L., Butts, D. A. & Nienborg, H. Decision-related feedback in visual cortex
733 lacks spatial selectivity. *Nature Communications* **12**, 1–11 (2021).
- 734 58. Kang, I. & Maunsell, J. H. R. The Correlation of Neuronal Signals with Behavior at Different Levels
735 of Visual Cortex and Their Relative Reliability for Behavioral Decisions. *Journal of Neuroscience*
736 **40**, 3751–3767 (2020).
- 737 59. Seidemann, E. & Geisler, W. S. Linking V1 Activity to Behavior. *Annu. Rev. Vision* **4**, 287–310
738 (2018).
- 739 60. Cumming, B. G. & Nienborg, H. Feedforward and feedback sources of choice probability in neural
740 population responses. *Curr Opin Neurobiol* **37**, 126–132 (2016).
- 741 61. Roelfsema, P. R. & Spekreijse, H. The representation of erroneously perceived stimuli in the
742 primary visual cortex. *Neuron* **31**, 853–863 (2001).
- 743 62. Roelfsema, P. R. & de Lange, F. P. Early Visual Cortex as a Multiscale Cognitive Blackboard. *Annu*
744 *Rev Vis Sci* **2**, 131–151 (2016).
- 745 63. Lyamzin, D. R., Aoki, R., Abdolrahmani, M. & Benucci, A. Probabilistic discrimination of relative
746 stimulus features in mice. *Proceedings of the National Academy of Sciences* **118**, e2103952118
747 (2021).
- 748 64. Saxena, S. *et al.* Localized semi-nonnegative matrix factorization (LocaNMF) of widefield calcium
749 imaging data. *PLoS Comp. Biol.* **16**, e1007791 (2020).
- 750 65. Li, N., Daie, K., Svoboda, K. & Druckmann, S. Robust neuronal dynamics in premotor cortex during
751 motor planning. *Nature* **532**, 459–464 (2016).
- 752 66. Aoki, R., Tsubota, T., Goya, Y. & Benucci, A. An automated platform for high-throughput mouse
753 behavior and physiology with voluntary head-fixation. *Nature Communications* **8**, (2017).
- 754 67. Burgess, C. P. *et al.* High-yield methods for accurate two-alternative visual psychophysics in head-
755 fixed mice. *Cell Rep.* **20**, 2513–2524 (2017).
- 756 68. Wang, Q. *et al.* The allen mouse brain common coordinate framework: A 3D reference atlas. *Cell*
757 **181**, 936-953.e20 (2020).
- 758 69. Lyamzin, D. & Benucci, A. The mouse posterior parietal cortex: Anatomy and functions.
759 *Neuroscience Research* **140**, (2019).
- 760 70. Averbeck, B. B. & Lee, D. Effects of noise correlations on information encoding and decoding. *J*
761 *Neurophysiol* **95**, 3633–3644 (2006).

- 762 71. Seung, H. S. & Sompolinsky, H. Simple models for reading neuronal population codes. *Proc Natl*
763 *Acad Sci U S A* **90**, 10749–10753 (1993).
- 764 72. Ohki, K. *et al.* Highly ordered arrangement of single neurons in orientation pinwheels. *Nature*
765 **442**, 925–928 (2006).
- 766 73. Couto, J. *et al.* Chronic, cortex-wide imaging of specific cell populations during behavior. *Nature*
767 *Protocols* **16**, 3241–3263 (2021).
- 768 74. Sommer, M. A. & Wurtz, R. H. Brain circuits for the internal monitoring of movements. *Annu. Rev.*
769 *Neurosci.* **31**, 317–338 (2008).
- 770 75. Esterman, M. & Rothlein, D. Models of sustained attention. *Current Opinion in Psychology* vol. 29
771 174–180 (2019).
- 772 76. Sarter, M., Givens, B. & Bruno, J. P. The cognitive neuroscience of sustained attention: where
773 top-down meets bottom-up. *Brain research reviews* **35**, 146–160 (2001).
- 774 77. Unsworth, N., Robison, M. K. & Miller, A. L. Pupillary correlates of fluctuations in sustained
775 attention. *Journal of cognitive neuroscience* **30**, 1241–1253 (2018).
- 776 78. Pho, G. N., Goard, M. J., Woodson, J., Crawford, B. & Sur, M. Task-dependent representations of
777 stimulus and choice in mouse parietal cortex. *Nat Commun* **9**, 2596 (2018).
- 778 79. Kiani, R. & Shadlen, M. N. Representation of confidence associated with a decision by neurons in
779 the parietal cortex. *Science* **324**, 759–764 (2009).
- 780 80. Yang, G. R., Joglekar, M. R., Song, H. F., Newsome, W. T. & Wang, X. J. Task representations in
781 neural networks trained to perform many cognitive tasks. *Nat. Neurosci.* **22**, 297–306 (2019).
- 782 81. Mante, V., Sussillo, D., Shenoy, K. v & Newsome, W. T. Context-dependent computation by
783 recurrent dynamics in prefrontal cortex. *Nature* **503**, 78–84 (2013).
- 784 82. Haefner, R. M., Berkes, P. & Fiser, J. Perceptual decision-making as probabilistic inference by
785 neural sampling. *Neuron* **90**, 649–660 (2016).
- 786 83. Lee, T. S. & Mumford, D. Hierarchical Bayesian inference in the visual cortex. *J. Opt. Soc. Am. A*
787 *Opt. Image Sci. Vis.* **20**, 1434–1448 (2003).
- 788 84. Parker, A. J. & Newsome, W. T. Sense and the single neuron: probing the physiology of
789 perception. *Annu Rev Neurosci* **21**, 227–277 (1998).
- 790 85. Grujic, N., Brus, J., Burdakov, D. & Polania, R. Rational inattention in mice. *bioRxiv*
791 2021.05.26.445807 (2021) doi:10.1101/2021.05.26.445807.
- 792 86. McAdams, C. J. & Reid, R. C. Attention modulates the responses of simple cells in monkey
793 primary visual cortex. *J Neurosci* **25**, 11023–11033 (2005).
- 794 87. Angelucci, A. *et al.* Circuits and Mechanisms for Surround Modulation in Visual Cortex. *Annu Rev*
795 *Neurosci* (2017) doi:10.1146/annurev-neuro-072116-031418.
- 796 88. Keller, G. B. & Mrsic-Flogel, T. D. Predictive Processing: A Canonical Cortical Computation. *Neuron*
797 vol. 100 424–435 (2018).

- 798 89. Elsayed, G. F., Lara, A. H., Kaufman, M. T., Churchland, M. M. & Cunningham, J. P. Reorganization
799 between preparatory and movement population responses in motor cortex. *Nat. Comms.* **7**,
800 13239 (2016).
- 801 90. Ohki, K., Chung, S., Ch'ng, Y. H., Kara, P. & Reid, R. C. Functional imaging with cellular resolution
802 reveals precise micro-architecture in visual cortex. *Nature* (2005).
- 803 91. Ungerleider, L. M. & Mishkin, M. Two cortical visual systems. in *Analysis of Visual Behavior* (eds.
804 Ingle, D. J., Goodale, M. A. & Mansfield, R. J. W.) (MIT Press, 1982).
- 805 92. Siegel, M., Buschman, T. J. & Miller, E. K. Cortical information flow during flexible sensorimotor
806 decisions. *Science* **348**, 1352–1355 (2015).
- 807 93. Aoi, M. C., Mante, V. & Pillow, J. W. Prefrontal cortex exhibits multidimensional dynamic
808 encoding during decision-making. *Nature Neuroscience* 1–11 (2020) doi:10.1038/s41593-020-
809 0696-5.
- 810 94. Kaufman, M. T., Churchland, M. M., Ryu, S. I. & Shenoy, K. v. Cortical activity in the null space:
811 permitting preparation without movement. *Nat Neurosci* **17**, 440–448 (2014).
- 812 95. Song, H. F., Yang, G. R. & Wang, X.-J. Training Excitatory-Inhibitory Recurrent Neural Networks for
813 Cognitive Tasks: A Simple and Flexible Framework. *PLoS Comput Biol* **12**, e1004792 (2016).
- 814 96. Rolnick, D., Veit, A., Belongie, S. & Shavit, N. Deep learning is robust to massive label noise. *arXiv*
815 **1705.10694**, (2017).
- 816 97. Gold, J. I. & Shadlen, M. N. Neural computations that underlie decisions about sensory stimuli.
817 *Trends Cogn Sci* **5**, 10–16 (2001).
- 818 98. Bogacz, R. Optimal decision-making theories: linking neurobiology with behaviour. *Trends Cogn*
819 *Sci* **11**, 118–125 (2007).
- 820 99. Chung, S. & Abbott, L. F. Neural population geometry: An approach for understanding biological
821 and artificial neural networks. *arXiv* (2021).
- 822 100. Berezovskii, V. K., Nassi, J. J. & Born, R. T. Segregation of feedforward and feedback projections in
823 mouse visual cortex. *Journal of Comparative Neurology* **519**, 3672–3683 (2011).
- 824 101. Waters, J. Sources of widefield fluorescence from the brain. *eLife* **6**, 9-e59841 (2020).
- 825 102. Zagha, E. Shaping the Cortical Landscape: Functions and Mechanisms of Top-Down Cortical
826 Feedback Pathways. *Frontiers in Systems Neuroscience* **14**, 33 (2020).
- 827 103. Pachitariu, M. *et al.* Suite2p: beyond 10,000 neurons with standard two-photon microscopy.
828 *bioRxiv* (2017) doi:10.1101/061507.
- 829 104. Allen, W. E. *et al.* Global Representations of Goal-Directed Behavior in Distinct Cell Types of
830 Mouse Neocortex. *Neuron* **94**, 891-907.e6 (2017).
- 831 105. Marshel, J. H., Garrett, M. E., Nauhaus, I. & Callaway, E. M. Functional specialization of seven
832 mouse visual cortical areas. *Neuron* **72**, 1040–1054 (2011).
- 833 106. Waters, J. *et al.* Biological variation in the sizes, shapes and locations of visual cortical areas in the
834 mouse. *PLoS One* **14**, e0213924 (2019).

Acknowledgments

835 We thank Rie Nishiyama, Yuka Iwamoto, and Yuki Goya for providing technical support for multiple
836 aspects of the experiments. We also thank O'Hara & Co., Ltd. for their support with the equipment. This
837 work was funded by RIKEN BSI and RIKEN CBS institutional funding; HFSP postdoctoral fellowship
838 LT000582/2019 awarded to J. O.; JSPS grants 26290011, 17H06037, 372 C0219129 awarded to A. B.; and
839 a Fujitsu collaborative grant.

Authors contributions

840 A.B. and J. O. conceived the project and wrote the manuscript; J.O., M. A., R. A., and D. L. collected the
841 data; M. A. and J. O. pre-processed the data and J. O. analyzed the data.

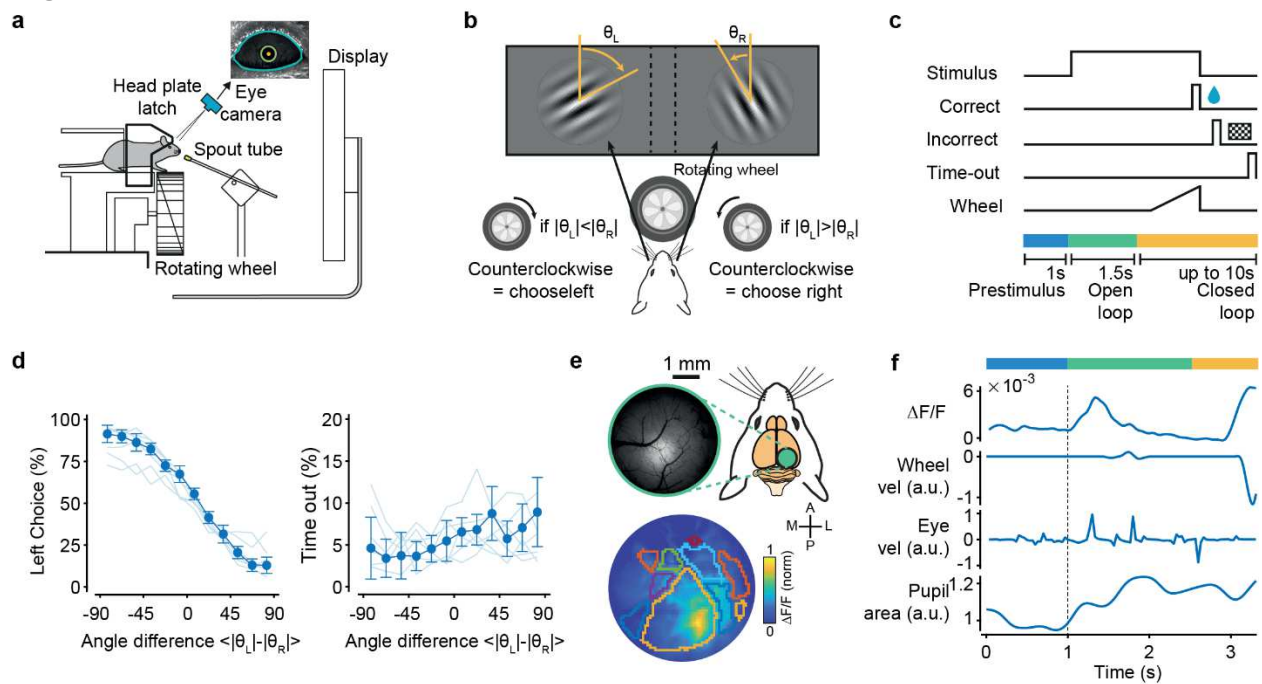
Data and code availability

842 Code for the analyses and source data for the figures will be made available upon acceptance of the
843 manuscript at <https://github.com/benuccilabncb/dm>. All other relevant data will be made available by
844 the corresponding author upon reasonable request.

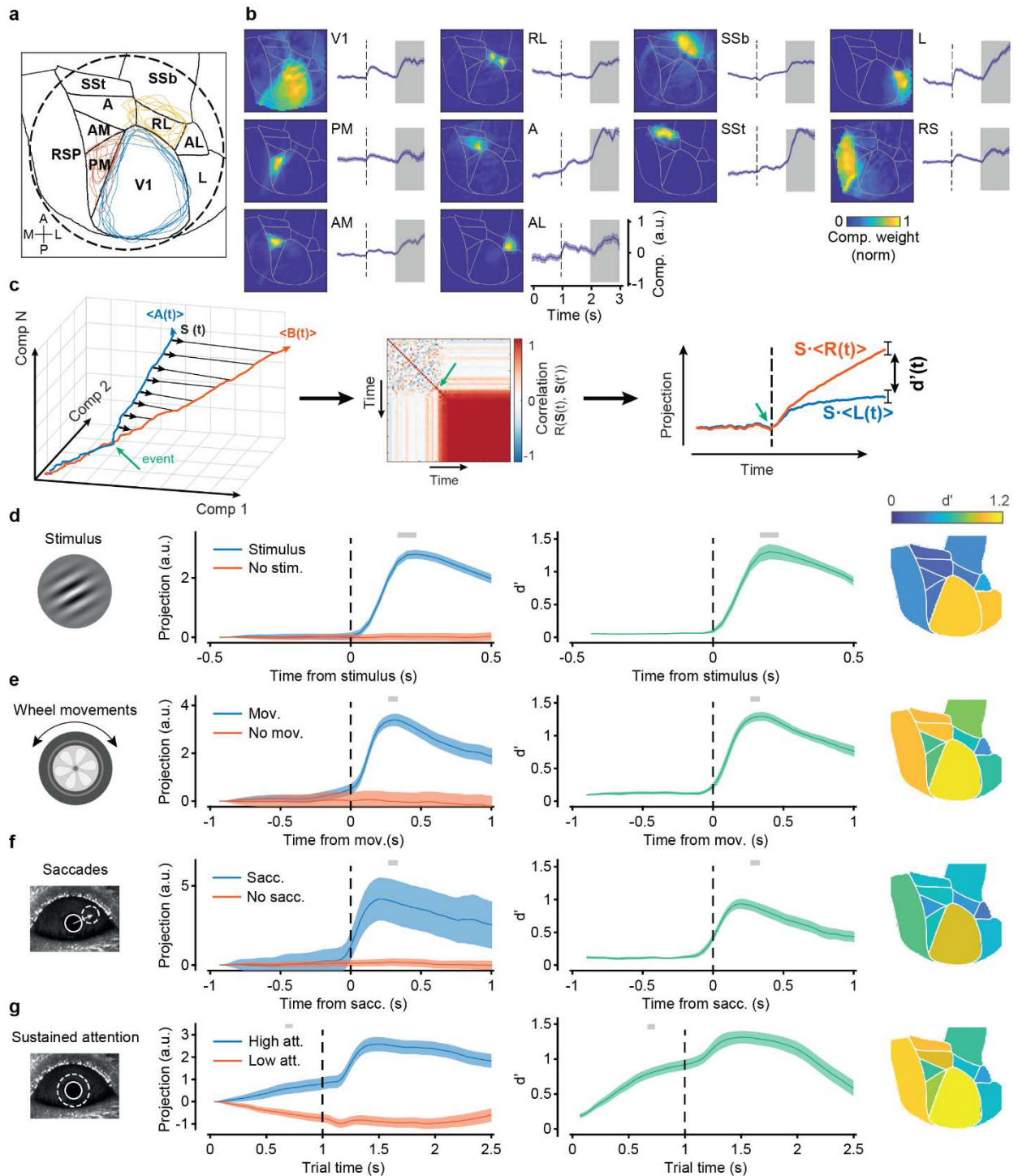
Competing Interests

845 The authors declare no competing interests.

Figures



846 **Figure 1 | Imaging the posterior cortex during an orientation discrimination task.** **a**, Mice were trained
 847 on a 2AFC orientation discrimination task using an automated setup featuring voluntary head fixation.
 848 They signaled a L/R choice by rotating a toy wheel with their front paws. **b**, Mice rotated the wheel to
 849 position the most vertical of two oriented gratings in the center of the screen. **c**, Trial structure: After a 1
 850 s pre-stimulus period, the stimulus was presented, followed by a 1.5 s open-loop (OL) interval in which
 851 wheel movements were decoupled from stimulus movements. Thereafter, in the closed-loop (CL) period,
 852 wheel rotations resulted in L/R horizontal shifts of the stimuli. Correct choices were rewarded with water;
 853 incorrect choices were followed by a checkerboard pattern presentation. Ten seconds of no movement in
 854 the CL period triggered a time-out period. **d**, Left: mice's performance in the task (fraction of left choices)
 855 as a function of relative angle difference from the target orientation (nominal value of zero), i.e., the task
 856 difficulty, averaging across trials with combinations of left and right angles associated to the same
 857 difficulty level. Thick line = mean (\pm s.e.) across animals; thin lines = individual animals. Right: fraction of
 858 timeout trials as a function of angle difference from the target orientation. Timeout trials did not depend
 859 on task difficulty. **e**, Widefield calcium imaging of the posterior cortices of Thy1-GCaMP6f mice, with
 860 retinotopic mapping of 10–12 visual areas (colored contours). **f**, Simultaneously recorded fluorescence
 861 signals (dF/F), wheel and eye velocities, and pupil area. In this example, choice was signaled at $t = 3.1$ s
 862 (by a sharp increase in wheel velocity). Dashed line represents the stimulus onset time.



863

864 **Figure 2 | LocaNMF decomposition identifies sensory, behavioral, and attention-related variables. a,**

865 Characteristic imaging window (dashed circle) superimposed on 10 cortical areas from the Allen Brain

866 Atlas reference framework. Blue, red, and yellow contours are the reference-aligned area boundaries for

867 V1, PM and RL for each animal. **b,** Spatial weights and trial-averaged time-series of the largest locaNMF

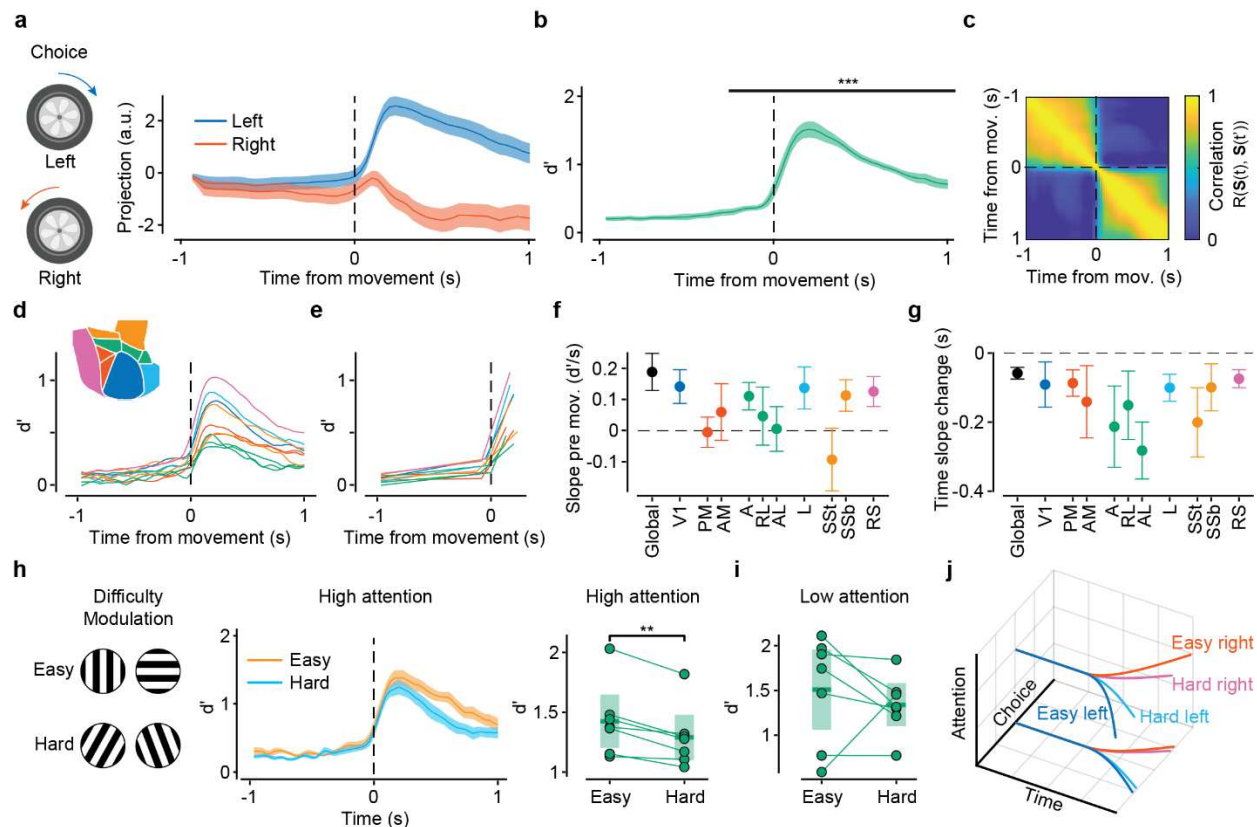
868 components for each of the 10 seeding regions (Supplementary Fig. 1a) for a representative animal. This

869 average consisted of trials with wheel movements within the 1 s shaded time interval, collectively for

870 clock-wise and cc-wise wheel rotations. Dashed lines denote stimulus onset. **c,** Schematic for the

871 definition of state axes. The direction of the state axis becomes stable after an event indicated by the

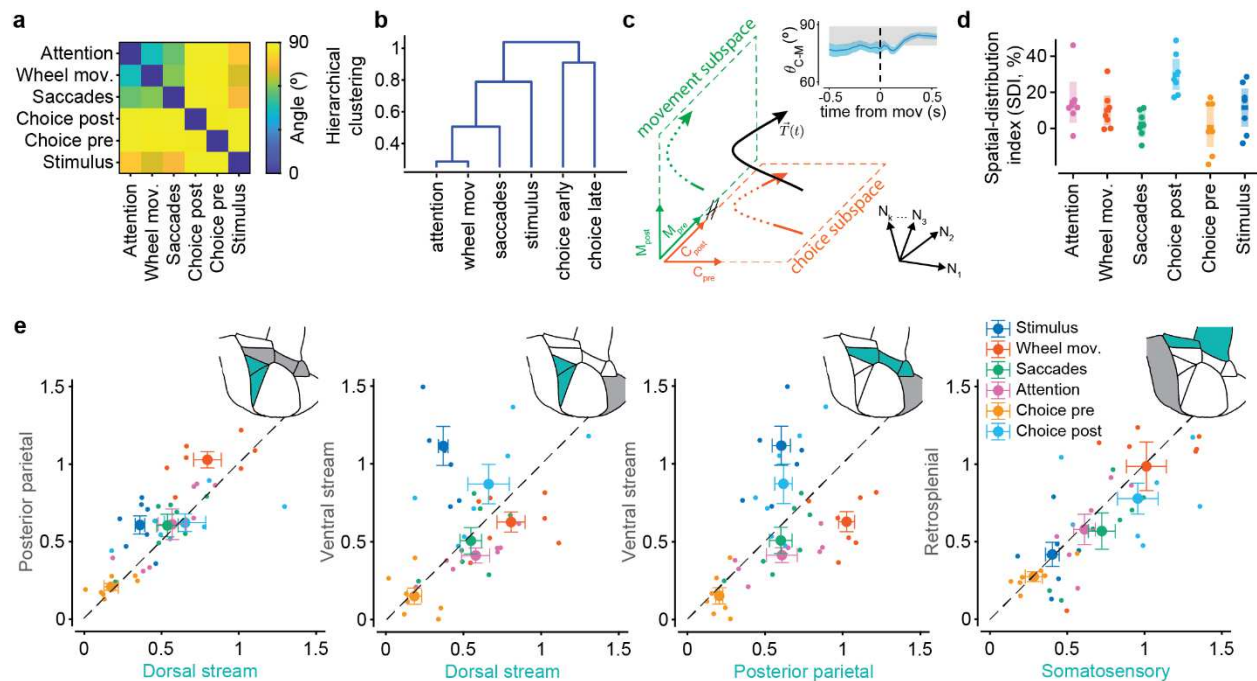
872 green arrow. Vector stability is measured as the temporal autocorrelation $r(\mathbf{S}(t), \mathbf{S}(t'))$, (right panel).
873 Projections (cross-validated) of the two variables $\mathbf{A}(t)$ and $\mathbf{B}(t)$ onto \mathbf{S} separately over time, as quantified
874 by a d' discriminability measure. **d**, Stimulus-related state axes. Left: projections of trials with and without
875 a stimulus response onto the stimulus state axis for a given animal. Lines and shaded regions indicate
876 across trial projection averages and standard error. Middle: Discriminability d' over time, averaged across
877 all animals. Gray bars on top, epoch used for the time-average of the state axis. Right: area-specific peak
878 d' scores obtained by defining the state axis using only the components originating from that area. **e**, As
879 in **d**, but aligned to movement-detection time, i.e., separability between trials with and without a detected
880 wheel movement. **f**, as in **e**, but for saccadic eye movements. **g**, As in **f**, but for sustained attention. Trials
881 with high and low levels of sustained attention were defined based on pupil area changes, using the
882 highest or lowest 33rd percentile of the area-change distribution.



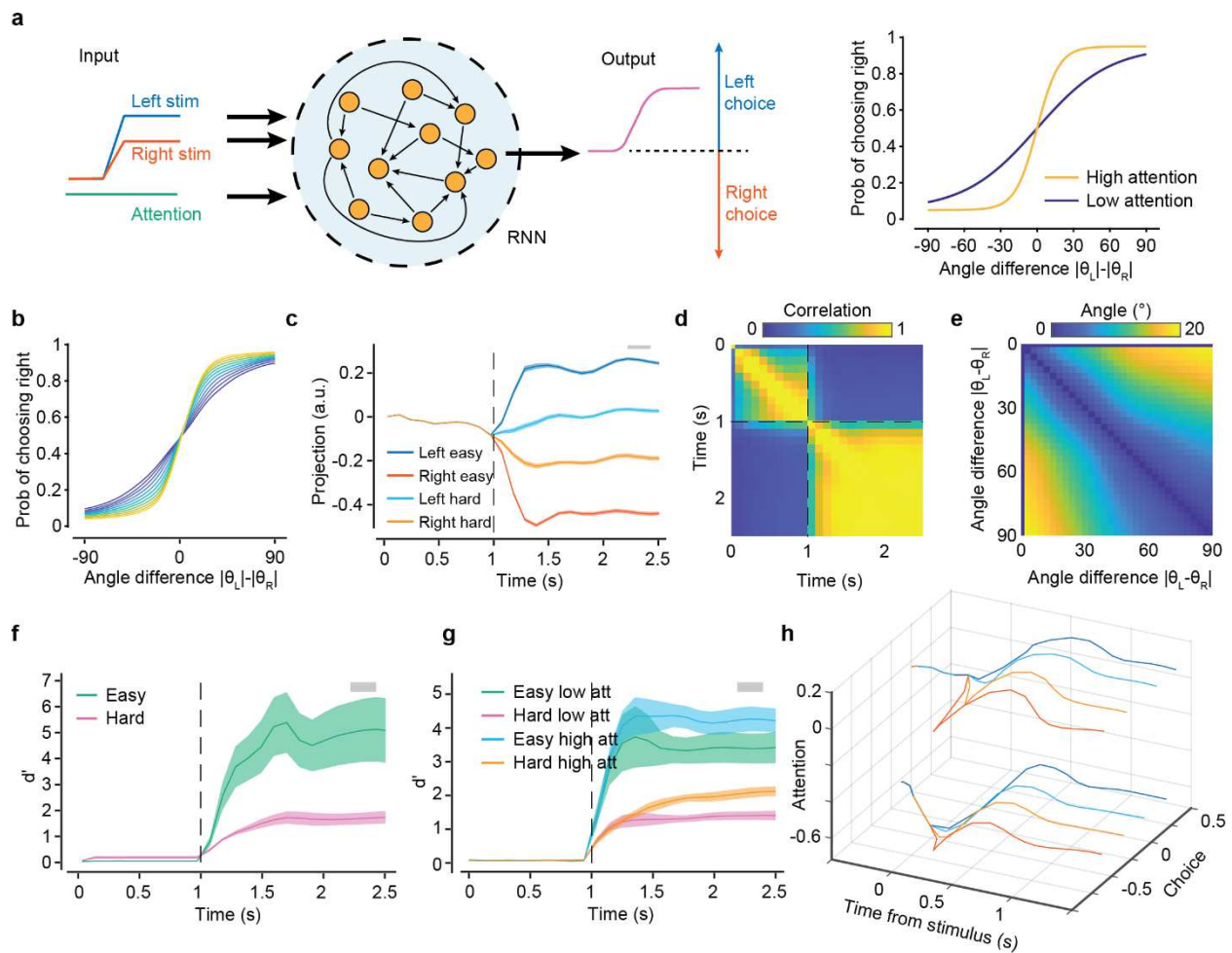
883

884 **Figure 3 | Choice signals have pre-motor component and are modulated by task difficulty and attention.**

885 **a**, Projections of left- and right-choice trials on the choice state axis for a characteristic animal (line for
 886 trial average and shaded area for s.e.). Wheel movements signaling either a left or a right choice were
 887 aligned to the wheel movement onset. **b**, Evolution of choice d' discriminability relative to movement
 888 time averaged across animals. d' values were significantly larger than baseline ($p < 0.001$, baseline defined
 889 between 1 and 0.5 s before movement onset, paired t-test) starting from 0.2 s before movement onset.
 890 **c**, Temporal stability of the state axis for choice, showing a clear change in the contribution of the choice
 891 state axis near the time of movement onset. Same animal as in **a**. **d**, Temporal evolution of area-specific
 892 d' curves (inset: area color code). **e**, Piecewise linear fits of the curves in **d** in pre- and post-movement
 893 periods. **f**, Pre-movement slopes fitted in **e** for different areas; error bars, 95% confidence intervals (CI)
 894 across animals ("global" indicates multi-area d'). **g**, Times of slope change for different areas from the fits
 895 in **e**. Data and colors as in **f**. **h**, Left: evolution of choice discriminability, d' , in high attention states for easy
 896 and hard trials (angle difference $>$ or $<$ 45°). Right: Paired comparisons of peak d' values for each animal
 897 ($p = 0.003$). **i**, As in **h**, but for low-attention states. Paired differences were not significant ($p = 0.50$). **j**,
 898 Schematic representation of the temporal evolution of left and right trajectories with difficulty and
 899 attention.



900
 901 **Figure 4 | Choice is distributed, near orthogonal to other components and with a ventral-stream**
 902 **dominance. a**, Angles between state axes averaged across animals. Choice axes (pre- and post-movement)
 903 were orthogonal to all other axes (smallest angle $84 \pm 7^\circ$). Attention and wheel had the smallest angular
 904 separation ($44 \pm 3^\circ$), followed by wheel and saccades ($56 \pm 4^\circ$). **b**, Hierarchical clustering from the angle
 905 distances in **a**. Attention and wheel movements were most similar. Choice pre- and post-movement onset
 906 clustered together, whereas stimulus and saccades had unique profiles. **c**, Schematic of the evolution of
 907 neural activity $\vec{T}(t)$ across movement and choice subspaces. In a multidimensional space of neural
 908 activations (N_1, \dots, N_k , black arrows), both movement and choice components (dotted arrows) projected to
 909 subspaces orthogonal to each other, defined by pre- and post-movement state axes (M_{pre}, M_{post} green,
 910 and C_{pre}, C_{post} orange). Axes in both subspaces were always orthogonal to each other (inset curve, angle
 911 between choice and movement state axes averaged across animals; shaded gray band is the expected
 912 angular distance range for statistically independent axes). **d**, Spatial-Distribution index (SDI) for each state
 913 axis. Choice had the largest SDI ($30 \pm 4\%$); dots are different animals; middle lines and shaded areas are
 914 means and 95% CI. **e**, We computed five d' values, each derived by restricting locaNMF components to
 915 one of the five area groups (insets), thus defining a 5-D space for d' components. The five broad area
 916 groups consisted of the dorsal stream (PM and AM), ventral stream (L), posterior parietal (A, AL and RL),
 917 somatosensory (SSt and SSb) and retrosplenial (RS) regions. Each dot corresponds to the d' values for a
 918 given animal and the large dot with errorbars to the average across animals and s.e.



919
 920 **Figure 5 | RNN model relates neural representations to DM computations.** **a**, Left: recurrent neural
 921 network (RNN) architecture consisting of a module with $N = 128$ recurrently connected units. The module
 922 receives two inputs for the left and right stimuli, and one input for the attentional state. It generates a
 923 continuous output that will determine the choice. Right: Target psychometric curves—matching the
 924 animals' psychometric responses—used to determine the proportion of L/R-choice trials in the training
 925 set for each difficulty level, depending on the attention state. **b**, Psychometric curves from the trained
 926 model showing that the model generalizes to intermediate values of attention and difficulty. **c**, Projection
 927 of L/R easy and hard trials onto the choice state axis following the same methods used in Fig. 2. Shaded
 928 bar at the top denotes the selected time used for state axis averaging. **d**, The choice axis became stable
 929 quickly after the stimulus presentation ($t = 1$ s). **e**, Angle difference between choice axes computed at
 930 different difficulty levels. Choice axes remained almost parallel to each other, with the largest deviation
 931 (between the easiest and most difficult conditions) smaller than 20° . **f**, Discriminability for choice (d') was
 932 higher in easy trials than in difficult trials. Line and shaded area are the mean and 95% CI across 10 trained
 933 networks with different random initializations. **g**, Choice was modulated by attention, as shown by the
 934 increase in discriminability values in trials with high attention levels. **h**, Diagram of the projected
 935 trajectories in the space spanned by the axes of choice and attention.

Supplementary Files

This is a list of supplementary files associated with this preprint. Click to download.

- [supplementarymaterial.pdf](#)